arXiv:1811.05551v1 [cond-mat.mes-hall] 13 Nov 2018

Phase locking of a pair of nano ferromagnetic oscillators on a topological insulator

Cheng-Zhen Wang,[1] Hong-Ya Xu,[1] Nicholas D. Rizzo,[2] Richard A. Kiehl,[1] and Ying-Cheng Lai[1,3,*]

[1]*School of Electrical, Computer and Energy Engineering, Arizona State University, Tempe, Arizona 85287, USA*
[2]*Northrop Grumman Corporation, Linthicum, Maryland 21090, USA*
[3]*Department of Physics, Arizona State University, Tempe, Arizona 85287, USA*

(Dated: November 29, 2021)

We investigate the magnetization dynamics of a pair of ferromagnetic insulators (FMIs) deposited on the surface of a topological insulator (TI). Due to the nonlinear nature of the underlying physics and intrinsic dynamics, the FMIs can exhibit oscillatory behaviors even under a constant applied voltage. The motion of the surface electrons of the TI, which obeys relativistic quantum mechanics, provides a mechanism of direct coupling between the FMIs. In particular, the spin polarized current of the TI surface electrons can affect the magnetization of the two FMIs, which in turn modulates the electron transport, giving rise to a hybrid relativistic quantum/classical nonlinear dynamical system. We find robust phase and anti-phase locking between the magnetization dynamics. As driving the surface electrons of a TI only requires extremely low power, our finding suggests that nano FMIs coupled by a spin polarized current on the surface of TI have the potential to serve as the fundamental building blocks of unconventional, low-power computing paradigms.

I. INTRODUCTION

There has been an increasing need to develop unconventional computing paradigms to deal with special tasks, such as rapid image recognition, with which conventional digital computing based on integrated circuits finds fundamental difficulties. Networks of nanoscale oscillators could provide the needed paradigm for such tasks, where extremely fast image recognition could potentially be realized with non-Boolean networks in which processing is done by local operations using analog techniques naturally suited to the task. Due to the inevitable power dissipation of the oscillators, it is desired to develop ultra-small oscillators based on a highly energy-efficient physical mechanism to realize energy efficient computing.

The history of computing with oscillators dates back to Goto[1] and von Neumann[2] who proposed to represent Boolean logic states by the electrical phase of an oscillator, rather than by the voltage or current level. Almost forty years later, an energy efficient implementation of this scheme based on single-electron tunneling oscillators, referred to as tunneling phase logic, was proposed[3,4]. The synchronization behavior of such pulse coupled oscillators opens the possibilities for non-Boolean computing[5] as well. Coupled nano-oscillators are also promising for combinatorial optimization problems such as vertex coloring of graphs[6] with applications in scheduling[7], resource allocation[8] and other computationally difficult (NP-hard) problems[9]. While tunneling phase logic was shown to be capable of both Boolean functions[10] and non-Boolean image processing operations[11], its physical mechanism was found to be too sensitive to thermal noise[12] for practical applications, calling for schemes to suppress noise[13] and alternative mechanisms for developing more robust nano-oscillators[14].

In general, the ability to control and manipulate magnetization dynamics is essential to developing spintronic memory, logic, and sensing nanodevices. A mechanism that has been extensively studied theoretically and experimentally is spin-transfer torque[15,16], which is based on the transfer of the spin angular momentum between a spin current flow and the local magnetization of a ferromagnetic layer. The mechanism can be exploited to develop, e.g., switching and steady precession of spin torque oscillators (STOs)[17,18]. The dynamics of precession of a single STO provide the basis for synchronizing a number of STOs[19–21], which has applications such as microwave power generation and sensing. Phase locking of two STOs has been achieved experimentally in spin torque devices with multiple nanocontacts, in which the magnetization in all the nanocontact regions can be locked at the same phase via a propagating spin wave[22–24]. Phase locking of STOs through coupled electrical circuits has also been studied in an array of STO nanopillars that can be electrically connected in series or in parallel[25–30]. In this case, the AC current produced by each individual oscillator leads to a feedback among the STOs, thereby realizing synchronization. In addition, synchronization can be achieved through magnetic dipolar coupling in perpendicular-to-plane polarized STOs[31]. Local synchronization between vortex-based STOs interacting with each other can occur through the mediation of closely spaced antivortices[32]. Recently, spin-torque and spin-Hall nano-oscillators[33] have gained attention for their potential applications in various non-Boolean computing[34] including image processing[35], associative memory, pattern recognition[36–38], and spatiotemporal wave computing[39]. Especially, the spin Hall effect[40–43] was exploited to experimentally realize synchronization of STOs driven by a pure spin current through microwave driving[44] and a method to synchronize multiple STOs without requiring any external AC excitation was proposed[45]. Existing studies on STOs have been focused primarily on nanocontact spin valves and magnetic tunnel junction pillar structures. While the junction structures appear

more promising for microwave power generation because of their high junction resistance and a larger magnetoresistance, nanocontact spin valves are more promising for mutual phase-locking among multiple STOs because of their better interdevice coupling geometry[22–24,46].

In this paper, motivated by the growing interest in exploiting topological quantum materials for achieving novel charge transport and efficient electrical control of magnetization in spintronics applications, we investigate whether it is possible to realize phase locking of nanoscale magnetic oscillators coupled via some topological mechanism, e.g., through a topologically protected current. This has the potential to lead to highly efficient, low power nano-oscillators as the fundamental building blocks of unconventional computing paradigms. To be concrete, we consider the prototypical setting of a pair of ferromagnetic insulators (FMIs) on the surface of a three-dimensional (3D) topological insulator (TI). A 3D TI possesses an insulating bulk but hosts chiral metallic channels on its surface, where electrons are described as massless Dirac fermions with spin-momentum locking[47,48], resulting in large spin-charge conversion efficiency[49–52]. The locking provides an effective mechanism to control FMI magnetization[53,54], and a large figure of merit for charge-spin conversion has been experimentally realized[55,56]. For a single FMI deposited on the top of a 3D TI, the exchange coupling between the magnetization and the surface state of TI can lead to nonlinear magnetization evolution but the spin-momentum locking of the surface current of the TI is preserved, and this can lead to phenomena such as anomalous magnetoresistance, unconventional transport behaviors[57,58], and magnetization switching due to Hall current induced effective anisotropy field[59–61]. Quite recently, steady self oscillations in the FMI/TI heterostructure were uncovered[62,63] and explained[64], and a number of nonlinear dynamical behaviors were studied[65,66]. Here, we apply a DC voltage to the TI and place the two FMIs on the top of the TI in series. We first consider the case where the distance between the two FMIs is larger than the de Broglie wavelength so that quantum interference between the two FMIs can be neglected. As a result, the surface electronic states provide the only mechanism that couples the two FMIs. We calculate the average spin of the electron flow in each heterostructure interface by solving the quantum transmission. The effective spin field, when combined with the magnetic anisotropy of the FMIs, can lead to self oscillations of the magnetization vectors of the FMIs, *even when the external driving is DC*. The oscillations in turn can modulate the electron transmission periodically, effectively making the current time varying. The resulting AC current provides the needed coupling between the two FMIs for phase locking. We then study the case where there is quantum interference between the two FMIs and find robust phase locking. The topologically coupled FMI system thus represents a class of highly efficient, low power nanoscale coupled oscillators, which can potentially serve as the fundamental building blocks for unconventional computing paradigms.

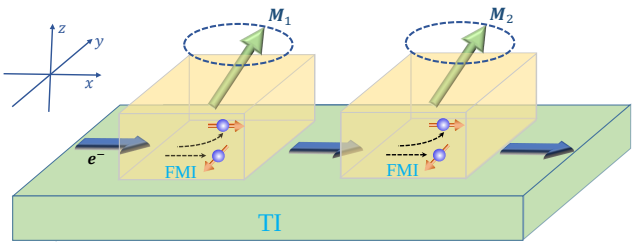


FIG. 1. **Schematic illustration of two FMIs on the top of a TI**. The two yellow blocks represent the FMIs and the green block underneath is the TI. The green arrows in the yellow blocks are the magnetization vectors $\boldsymbol{M}$ and the blue arrows on the surface of green blocks represent certain electron incident direction in the magnetic free region. The small red arrows with the electrons (blue spheres) denote the spin direction and the black arrows indicate the direction of electron motion.

II. MODEL AND SOLUTION METHOD

Figure 1 shows schematically the system configuration of two FMIs deposited on the top of a TI[67,68], which can be realized using material combinations such as Bi_2Se_3/YIG ($Y_3Fe_5O_{12}$)[69], Bi_2Te_3/GdN[70], Bi_2Se_3/EuS[71,72], and Bi_2Se_3/$Cr_2Ge_2Te_4$[73]. (Appendix A provides more details about possible experimental realization.) The dynamical variable of each FMI is its macroscopic magnetization vector $\boldsymbol{M}$. For the TI, a topologically protected, spin polarized current flows through the surface, where the spin is perpendicular to the current flow direction. The spin and magnetization are coupled via proximity interaction. The magnetization can affect the spin distribution and hence the electron transport behavior. Simultaneously, the average spin will act as an effective magnetic field to influence the dynamics of the FMIs. Even with constant voltage driving, the magnetization vectors of the FMIs can exhibit oscillations. Intuitively, because the spin polarized current is common to both FMIs, it serves as a kind of coupling between the two FMIs. Specifically, the magnetization of the first FMI can affect the current, which in turn alters the effective magnetic field acting on the second FMI, impacting its dynamics, and vice versa. As a result, phase locking can arise.

To develop a computational model, we assume that the magnetization precession period is much longer than the time it takes for electronic transport through the FMI/TI interface. For simplicity, we first ignore the quantum interference effect or any other indirect interaction between the two FMIs. (The effect of quantum interference will be discussed in Sec. III 2.) We solve the time-

independent Dirac equation for the electrons at the two interfaces separately, taking into account the proximity effect. In particular, the low-energy electronic behavior of the TI surface states is described by the effective Dirac Hamiltonian[62]

$$H = \hbar v_F(\boldsymbol{\sigma} \times \boldsymbol{k}) \cdot \hat{\boldsymbol{z}} - \xi \boldsymbol{M} \cdot \boldsymbol{\sigma} - U, \tag{1}$$

where $\boldsymbol{p} = \hbar \boldsymbol{k} = -i\hbar(\partial_x, \partial_y, 0)$ is the two-dimensional (2D) electron momentum operator, $\boldsymbol{\sigma} = (\sigma_x, \sigma_y, \sigma_z)$ are the Pauli matrices for electron spin, $\hat{\boldsymbol{z}} = (0, 0, 1)$ is the unit vector normal to the TI surface, and v_F is the electron Fermi velocity, as shown in Fig. 1. The second term in Eq. (1) represents the energy of exchange interaction between an electron and the proximate FMI, with ξ being the coupling coefficient. The last term is the external bias applied to the interface regions. When quantum interference is neglected, we can treat the two FMI/TI heterostructures separately. Especially, we solve Eq. (1) by taking $\boldsymbol{M} = \boldsymbol{M}_1$ in the first heterostructure region and match the wavefunctions without the need to consider the influence of the second heterostructure. Similarly, the second heterostructure can be treated without considering any influence from the first one. The formulas for calculating the electron transmission through one FMI/TI heterostructure can be found in Appendix C. When quantum interference is taken into account, we solve Eq. (1) for the two FMIs as a whole - see Sec. III 2 and Appendix D for details.

The energy eigenvalues of Eq. (1) are

$$E_\pm = \pm\sqrt{(v_F p_x + \xi M_y)^2 + (v_F p_y - \xi M_x)^2 + \xi^2 M_z^2} - U,$$

where the "±" signs correspond to the conduction (+) and valence (−) bands, and $\boldsymbol{p} = \hbar \boldsymbol{k}$ is the electron momentum. We see that the in-plane (x, y) magnetization components can lead to a displacement in the momentum space. Especially, the momentum displacement in the y direction can lead to a Hall current in that direction. Besides, the perpendicular component of the magnetization vector can open up a gap between the Dirac cones, contributing an additional Hall current in y. The first kind of Hall current plays the role of effective anisotropy, while the second kind is responsible for anti-damping. The two kinds of Hall current can lead to self oscillations of magnetization[62–64].

For each FMI, the conductance through one FMI/TI heterostructure can be calculated from the Landauer-Buttiker formalism[58,62,74]:

$$G = \frac{Ee^2 L_w}{2\pi^2\hbar^2 v_F} \int_{-\frac{\pi}{2}}^{\frac{\pi}{2}} T_{\boldsymbol{M}}(E, \theta) \cos\theta d\theta. \tag{2}$$

where E is electron Fermi energy, $T_{\boldsymbol{M}}(E, \theta) = |t|^2$ is the transparency through one FMI/TI barrier, θ is the electron incident angle in the (x, y) plane, and $-e$ is the electron charge. For two coupled FMIs, their conductances G_1 and G_2 determine the voltage partition between them:

$$V_1 = \frac{G_2}{G_1 + G_2} V \quad \text{and} \quad V_2 = \frac{G_1}{G_1 + G_2} V. \tag{3}$$

The current density is given by

$$J_x = \frac{V_1 G_1}{L_w} = \frac{Ee^2 V_1}{2\pi^2\hbar^2 v_F} \int_{-\frac{\pi}{2}}^{\frac{\pi}{2}} T_{\boldsymbol{M}}(E, \theta) \cos\theta d\theta. \tag{4}$$

From the current definition[61,62] $\hat{J} = -e\nabla_{\boldsymbol{p}} H = -ev_F(-\hat{\sigma}_y, \hat{\sigma}_x)$, we can get the mean spin polarization density for the first FMI as

$$\langle \sigma_y \rangle_1 = J_x / ev_F, \tag{5}$$

$$= \frac{EeV_1}{2\pi^2\hbar^2 v_F^2} \int_{-\frac{\pi}{2}}^{\frac{\pi}{2}} T_{\boldsymbol{M}}(E, \theta) \cos\theta d\theta, \tag{6}$$

The following equality:

$$T_{\boldsymbol{M}}(E, \theta) \cos\theta = -\psi^\dagger \sigma_y \psi,$$

where ψ is the electron wavefunction, can be used in our derivation of the average spin density (a proof of this equality is presented in Appendix C). Specifically, using the equality, we have

$$\langle \sigma_y \rangle_1 = -\frac{EeV_1}{2\pi^2\hbar^2 v_F^2} \int_{-\frac{\pi}{2}}^{\frac{\pi}{2}} \psi^\dagger \sigma_y \psi d\theta$$

$$= -\frac{EeV_1}{2\pi^2\hbar^2 v_F^2 d} \int_0^d \int_{-\frac{\pi}{2}}^{\frac{\pi}{2}} \psi^\dagger \sigma_y \psi d\theta dx \tag{7}$$

There are three spin components for each electron at a specific position with certain incident angle: $\psi^\dagger \sigma_x \psi$, $\psi^\dagger \sigma_y \psi$, and $\psi^\dagger \sigma_z \psi$. Once the y component of the spin density is known, the other components can be obtained by replacing $\psi^\dagger \sigma_y \psi$ in Eq. (7) by $\psi^\dagger \sigma_x \psi$ and $\psi^\dagger \sigma_z \psi$. Note that the factor before the integral is related to the electron density. We have

$$\langle \sigma_x \rangle_1 = -\frac{EeV_1}{2\pi^2\hbar^2 v_F^2 d} \int_0^d \int_{-\frac{\pi}{2}}^{\frac{\pi}{2}} \psi^\dagger \sigma_x \psi d\theta dx, \tag{8}$$

$$\langle \sigma_z \rangle_1 = -\frac{EeV_1}{2\pi^2\hbar^2 v_F^2 d} \int_0^d \int_{-\frac{\pi}{2}}^{\frac{\pi}{2}} \psi^\dagger \sigma_z \psi d\theta dx. \tag{9}$$

Alternatively, we can get the electron density first and then obtain the spin density expression. A detailed discussion is presented in Appendix C.

The mean spin density for the second FMI can be obtained in a similar way. The effective magnetic field is then given by

$$\boldsymbol{B}_{spin} = -\langle \frac{\partial H}{\partial \boldsymbol{M}} \rangle \frac{A_0}{V_0} = \frac{\xi}{a} \langle \boldsymbol{\sigma} \rangle, \tag{10}$$

where $\langle \boldsymbol{\sigma} \rangle$ is the mean spin density of the electron flow.

In addition to the effective magnetic field contribution from the electron spin, there is another term that stems from the magnetic anisotropy of the material. We assume that the magnetic layer has z hard axis and x easy axis. The corresponding anisotropy parameters are

$K_z > K_y > K_x = 0$, and the density of the magnetic free energy[62] is given by

$$F(\boldsymbol{M}) = F_{an} + F_{spin} = K_x n_x^2 + K_y n_y^2 + K_z n_z^2 - \boldsymbol{M} \cdot \boldsymbol{B}_{spin}(\boldsymbol{M}), \quad (11)$$

where $\boldsymbol{n} = (n_x, n_y, n_z) = \boldsymbol{M}/|\boldsymbol{M}|$. The effective magnetic field due to material anisotropy can be obtained via $\boldsymbol{B}_{an} = -\partial F_{an}/\partial \boldsymbol{M}$.

The LLG equations for magnetization dynamics of the two coupled FMIs are

$$\frac{d\boldsymbol{n}_1}{dt} = -\gamma \boldsymbol{n}_1 \times \boldsymbol{B}_{eff}^{(1)}(\boldsymbol{n}_1, \boldsymbol{n}_2) + \alpha \boldsymbol{n}_1 \times \frac{d\boldsymbol{n}_1}{dt}, \quad (12)$$

$$\frac{d\boldsymbol{n}_2}{dt} = -\gamma \boldsymbol{n}_2 \times \boldsymbol{B}_{eff}^{(2)}(\boldsymbol{n}_1, \boldsymbol{n}_2) + \alpha \boldsymbol{n}_2 \times \frac{d\boldsymbol{n}_2}{dt}, \quad (13)$$

where the normalized magnetization vectors are $\boldsymbol{n}_1 = \boldsymbol{M}_1/|\boldsymbol{M}|$ and $\boldsymbol{n}_2 = \boldsymbol{M}_2/|\boldsymbol{M}|$, γ is the gyromagnetic ratio, and α is the Gilbert damping constant. The quantities $\boldsymbol{B}_{eff}^{(1)}$ and $\boldsymbol{B}_{eff}^{(2)}$ are the effective magnetic fields for the first and second FMI, respectively, with $\boldsymbol{B}_{eff}^{(1)} = \boldsymbol{B}_{spin}^{(1)} + \boldsymbol{B}_{an}^{(1)}$ and $\boldsymbol{B}_{eff}^{(2)} = \boldsymbol{B}_{spin}^{(2)} + \boldsymbol{B}_{an}^{(2)}$. The anisotropy induced effective magnetic fields $\boldsymbol{B}_{an}^{(1)}$ and $\boldsymbol{B}_{an}^{(2)}$ are different for the two FMIs, leading to different oscillation frequencies for the two FMIs under the same applied voltage. The spin induced effective magnetic field of the first heterostructure is $\boldsymbol{B}_{spin}^{(1)} = \xi \langle \boldsymbol{\sigma} \rangle_1 / a \sim V_1$, where V_1 is determined by the conductances of both heterostructures via voltage partition with the same longitudinal current in the x direction. The conductances are related to the magnetization vectors $\boldsymbol{M}_1$ and $\boldsymbol{M}_2$. Similarly, the spin induced effective magnetic field in the second heterostructure is $\boldsymbol{B}_{spin}^{(2)} \sim V_2$, which is related to $\boldsymbol{M}_1$ and $\boldsymbol{M}_2$ in the same way as for the first heterostructure. The magnetization vectors of the two FMIs are thus effectively coupled together via the common current on the surface of the TI.

The coupled magnetization dynamics can be solved by an iterative procedure. Firstly, with the magnetization vectors $\boldsymbol{M}_1$ and $\boldsymbol{M}_2$ of the two FMIs, we solve the Hamiltonian (1) to obtain the corresponding electron wavefunctions in the two heterostructures. Secondly, from the wavefunctions, we calculate the conductance [Eq. (2)] and the average spin. Using the common coupling current in the x direction through the two heterostructures, we carry out a simple voltage partition [Eq. (3)]. Thirdly, we calculate the spin density [Eqs. (7-9)] and obtain the effective magnetic field by spin, which affects the magnetization dynamics. These steps are repeated to obtain the time evolution of the magnetization vectors. A flow chart illustrating the iterative method for the two cases where quantum interference is absent and present, respectively, is provided in Appendix B.

Our simulation parameters are the following. Each magnet is assumed to have the dimension of d (length) $\times L_w$ (width) $\times a$ (thickness) $= 40 \times 90 \times 2.2$ nm^3, with hard-axis anisotropy coefficients $K_y = 2.0 \times 10^5$ erg/cm^3 and $K_z = 2.5 \times 10^5$ erg/cm^3 along the y and z axis, respectively. The initial magnetization is $M_0 = 1200$ Oe. The Gilbert damping factor is $\alpha = 0.01$. For the TI layer, the Fermi velocity of the electron is $v_F = 4.6 \times 10^7$ cm/s. The exchange energy term is $\xi M_0 = 40$ meV.

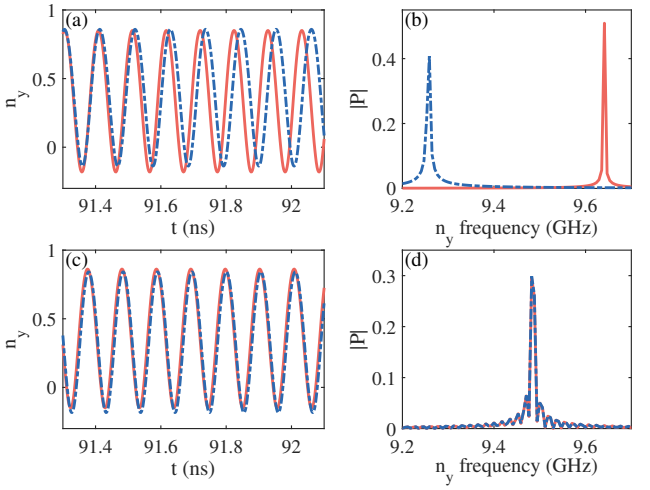


FIG. 2. **Phase locking between magnetization vectors of two FMIs**. For $K_y = 2 \times 10^4$ erg/cm^3 and electron energy 100 meV, (a) time evolution of the y components of magnetization vectors of the two isolated FMIs under the same applied voltage of 40 mV. The red solid and blue dashed curves denote the y components of the magnetization of the first and second FMI, respectively. (b) Fourier spectra of the time series in (a). (c,d) The corresponding results with coupling through the surface current of the TI under an applied voltage of 80 mV. There is phase locking.

III. RESULTS

1. *Phase locking in the absence of quantum interference*

To uncover phase locking for a pair of coupled FMIs in a general setting, we assume that the FMIs have different values of anisotropy: one with the values listed at the end of Sec. II and the other having an additional amount of anisotropy in the x direction with the value of the anisotropy coefficient being $K_x = 0.0955 \times 10^5$ erg/cm^3. Nonidentical values of the anisotropy lead to different oscillation frequencies for the two FMIs under the same applied voltage.

We first consider the case of isolated FMIs by applying the same DC voltage on the two FMIs separately. Figure 2(a) shows that the magnetization vectors of the isolated FMIs exhibit oscillations at difference frequencies, where the solid red and dotted blue curves correspond to the first and second FMI, respectively. Note that the two magnetization components deviate within

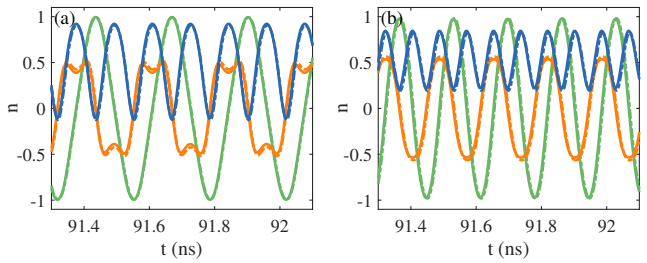


FIG. 3. **Robustness of phase locking for different parameter settings**. For $K_y = 1.5 \times 10^4$ erg/cm^3 (the anisotropy coefficient in y) and electron energy 100 meV, (a) phase locking between the two FMIs under voltage 100 mV. The red, blue and green curves denote the n_x, n_y and n_z components, respectively. The solid and dashed curves are for the first and second FMIs, respectively. (b) For applied voltage 140 mV, phase locking behavior when the damping factor is increased to 0.02 (from the value of 0.01 in Fig. 2).

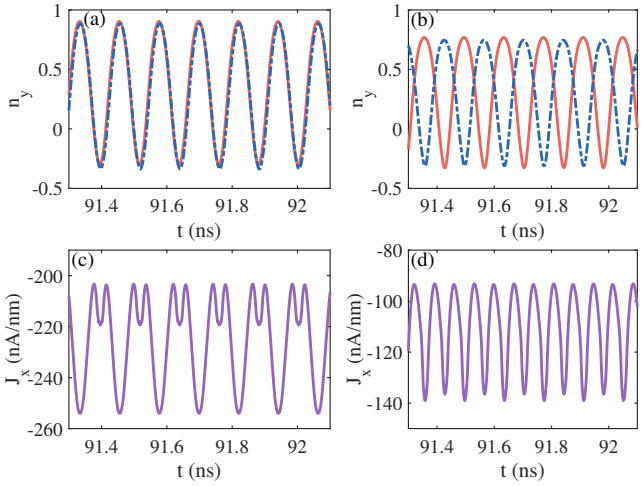


FIG. 4. **Phase and anti-phase locking between a pair of coupled FMIs**. (a) Phase locking between the y components of the magnetization vectors for $V_0 = 110$ mV and $E = 60$ meV. (b) Anti-phase locking for $V_0 = 190$ mV and $E = 30$ meV. (c,d) The corresponding evolutions of the surface current of the TI for cases (a,b), respectively. Other parameters are the same as those in Fig. 2(c).

1 ns (containing several oscillation periods), signifying a difference in their frequencies due to the difference in the anisotropy. The frequency difference can also be seen from the Fourier spectra, as shown in Fig. 2(b). For the second FMI with an additional value of anisotropy along the x axis, the frequency is lower than that of the first one. We next introduce coupling by placing the two FMIs in series on a TI and letting the current go through the two FMIs, as illustrated in Fig. 1. The separation between the two FMIs is sufficiently large, so that any quantum interference between the two FMIs can be neglected. We apply the voltage of 80 mV. The magnetization oscillations will make the current oscillate in time through the proximity effect, i.e., modulation of the transmission of electrons. The current induces an interaction between the two FMIs through an effective magnetic field due to electron spin, leading to phase locking, as shown in Fig. 2(c), where the y components of the magnetization vectors of the two FMIs evolve with time at the same pace. Phase locking can be further demonstrated by the Fourier spectra, as shown in Fig. 2(d), where the two oscillatory time series have essentially the same peak frequency. We have examined a large number of combinations of the parameters such as the amount of anisotropy and damping factor, and found robust phase locking in all cases, as exemplified in Fig. 3.

We also find persistent phase locking in wide ranges of the applied voltage and electron Fermi energy. For example, Figs. 4(a,b) demonstrate phase locking for two cases where the applied voltage and electron energy are (110 mV, 60 meV) and (190 mV, 30 meV), respectively, with other parameters being the same as those in Fig. 2(c). Note that in Fig. 4(a), the magnetization vectors of the two FMIs are in phase, while there is anti-phase locking between them in Fig. 4(b). The corresponding surface current oscillations in the TI are shown in Figs. 4(c,d). In each case, the primary frequency of the current oscillations is the same as that of the magnetization oscillations. To our knowledge, the demonstrated phase and anti-phase locking behaviors enabled by the proximity induced torques in the FMI/TI systems have not been reported before.

To examine more closely the different phase and anti-phase locking behaviors in Fig. 4, we plot the 3D trajectories of the magnetization unit vector. Figures 5(a,b) correspond to the cases in Figs. 4(a,b), respectively. The red and blue trajectories are for the two FMIs, and the red and blue dots denote the positions of the magnetization vector at certain time. For case (a), the trajectories almost coincide with each other and the magnetization vectors (red and blue dots) are at the same location for any time, and the frequency of the y component is twice those of the n_x and n_z components, as illustrated in insets (c,d). For case (b), the trajectories are close to each other but the magnetization vectors are dominated by the z component and have opposite phases at the time instants t_0 and t_1. In this case, the frequencies of the three components are the same. We also plot the trajectory of one FMI in the spherical coordinate, as shown in Fig. 6, where the components of the magnetization vector are $n_x = \cos\theta\cos\phi$, $n_y = \cos\theta\sin\phi$, and $n_z = \sin\theta$. The spherical coordinate trajectory in Fig. 6(a) corresponds to the case in Fig. 5(a), where the magnetization vector circulates about the minimum energy point. In Fig. 6(b), the trajectory is along the edge.

The difference in the trajectories is closely related to the relative value of the electron and exchange coupling energies. As illustrated in Fig. 7, when the magnetization vector is along the z direction, the exchange coupling energy is 40 meV, opening up a gap in the energy band. For the case where the electron energy is above the bot-

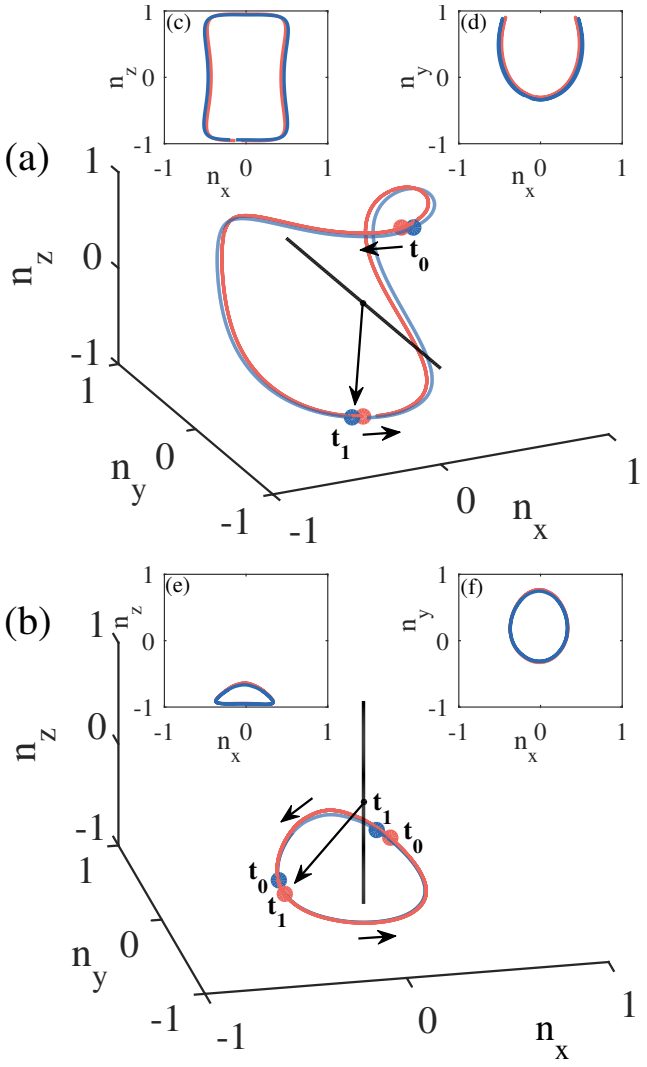


FIG. 5. **Trajectories of the magnetization unit vectors**. (a) Trajectories (red and blue for the two FMIs, respectively) in the 3D magnetization space corresponding to Fig. 4(a). The black arrow denotes the trajectory evolution direction. The insets (c,d) correspond to the projections of the trajectory on the $n_x - n_z$ and $n_x - n_y$ planes, respectively. (b) Trajectories corresponding to Fig. 4(b).

tom of the upper band (e.g., for energy value of 60 meV), the in-plane electron spin component is large, especially along the y axis. The value of the out-of-plane spin component is limited by the small exchange coupling energy in comparison with the electron energy. This has been confirmed by the effective magnetic field value from the average spin, as shown in Fig. 8(a). It can be seen that the absolute value of the effective magnetic field is stable and large along the y axis, whereas the z component exhibits large oscillations. The effective magnetic field by anisotropy makes the magnetization vector circulate about the y axis. When the electron energy is decreased to, say, 30 meV (an energy value inside the gap), the electron will experience a strong barrier if the z component of the magnetization vector is non-zero, leading to a large out-of-plane spin component that in turn acts as an effective magnetic field in the z direction. As a result, the total effective magnetic field is large in the z direction, causing the magnetization vector to precess dominantly about the z axis. This picture is confirmed by the effective magnetic field value experienced by the electron, as shown in Fig. 8(b), where the z component of the field is quite large.

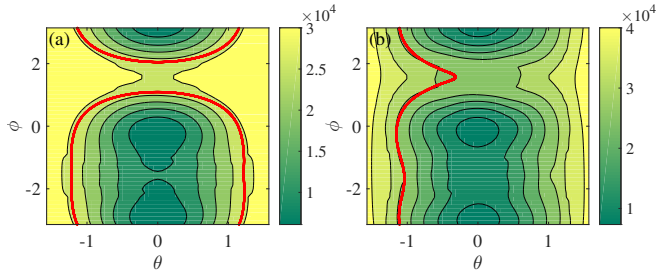


FIG. 6. **Magnetization trajectories in the spherical coordinate with respect to energy distribution**. The red curve is the trajectory of the magnetization vector. Darker background color indicates lower energy value. The applied voltage is 55 meV for (a) and 95 meV for (b), whereas the electron energy is 60 meV for (a) and 30 meV for (b).

When there is coupling between the two oscillators by the electron current in the TI, the magnetization vector will be mostly in-plane. In this case, the anti-damping torque will assume a relatively small value if there is anti-phase locking between the two magnetization vectors. As a result, in-phase locking will induce large fluctuations in both y and z components, as can be seen from Fig. 8(a), where the lower values of the y component correspond to a large absolute value in the z direction. On the contrary, if the out-of-plane spin component dominates, an anti-damping torque will arise, reducing the total current fluctuations.

2. *Effect of quantum interference on phase locking*

Having uncovered the phenomena of phase and anti-phase locking in a pair of FMIs coupled by the spin polarized surface current of the TI, we address the issue of quantum interference and investigate its effect on the phase locking dynamics. To take into account quantum interference, we treat the two FMIs as a single tunneling system and calculate the probability of quantum tunneling through the whole system.

Consider a surface electron in the TI moving toward the interface region. As shown in Fig. 9, there are five subregions of interest: (I) the "free" region to the left of the interface between the first FMI and TI, (II) the interface region itself, (III) the region between the two interfaces, (IV) the second interface region, and (V) the "free" region to the right of the region IV. Let θ be the incident angle of the electron from region I to region II.

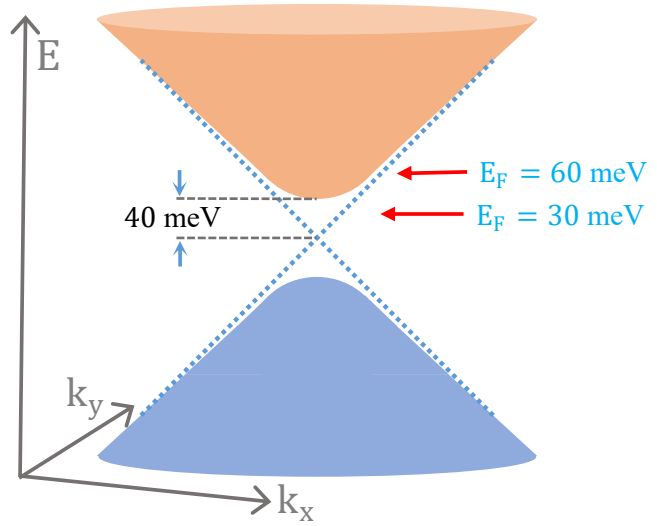


FIG. 7. **Electron energy band structure** for the case where the magnetization vector is in the z direction.

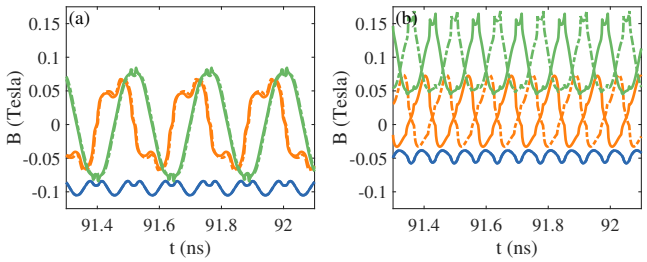


FIG. 8. **Effective magnetic field by spin**. The red, blue and green curves denote the effective magnetic field in the x, y and z directions, respectively. The solid and dashed curves are for the two FMIs. The two cases are: (a) $E = 60$ meV (above the bottom of the upper band, the upper horizontal red arrow in Fig. 7) and (b) $E = 30$ meV (in the gap, the lower horizontal red arrow in Fig. 7).

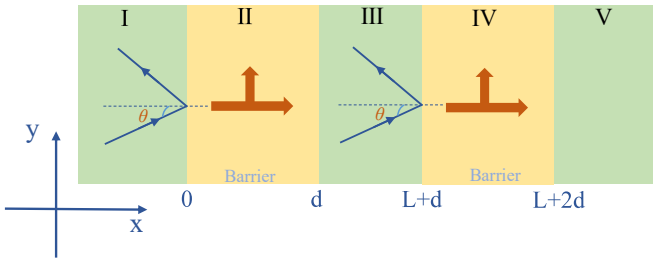


FIG. 9. **A schematic illustration of distinct quantum transport regions for calculating the effective coupling field**. The distance between the two FMIs is $L = d = 40$ nm.

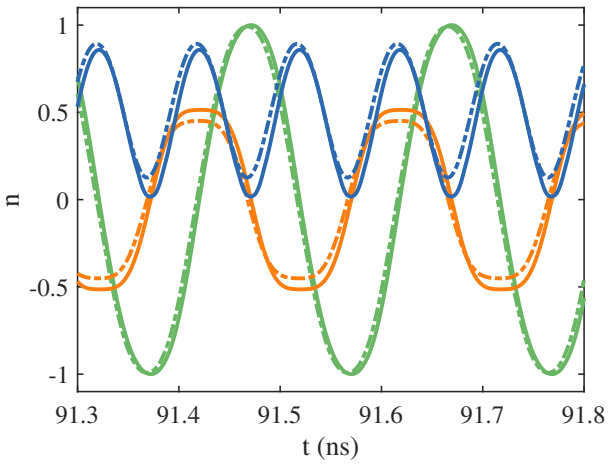


FIG. 10. **Phase locking between the two coupled FMIs in the presence of quantum interference**. The applied voltage is 50 mV and the electron energy is 100 meV. The red, blue and green curves denote n_x, n_y and n_z, respectively. The solid and dashed curves are for the FMI in region II and IV, respectively.

Solving the Dirac equation in each subregion, we obtain the spinor wavefunctions in the five regions, as listed in Appendix D. Matching the wavefunctions at the boundaries, we obtain all the coefficients and hence the wavefunction in the whole 2D space. The average spin polarization in each subregion and the corresponding effective magnetic field can then be calculated, as in Eqs. (4)-(13).

Figure 10 shows the representative magnetization dynamics of the two FMIs when quantum interference is taken into account (for $V_0 = 50$ mV and $E = 100$ meV). The three components of the magnetization vector are represented by different colors, and the solid and dashed curves are for the first and second FMI, respectively. The magnetization vectors exhibit oscillations and there is phase locking. We vary the external voltage and the electron energy and also change the anisotropy value. In all cases, persistent phase locking is observed.

IV. CONCLUSION

To summarize, motivated by the need for nanoscale oscillators for developing potential unconventional computing paradigms, we have studied the oscillatory dynamics and phase locking of a pair of FMI oscillators coupled through the spin-polarized current on the surface of an TI. The dynamics of the whole system are of the hybrid type[66]: a combination of classical nonlinear and relativistic quantum dynamics, with the following underlying physics. For each heterostructure interface between the FMI and TI, there is an average spin of the electron flow, which can be solved via the transmission through the interface. The average spin acts as an effective field which, when combining with the magnetic anisotropy of

the FMI, leads to self oscillations in the magnetization of each individual, uncoupled FMI. The self oscillations in turn modulate the electron transmission periodically, making the surface current of the TI time varying. The AC current generates the coupling between the two FMIs. As a result, stable phase or anti-phase locking between the two FMIs emerges, regardless of whether quantum interference is absent or present. The phase locking phenomenon is robust as it occurs in wide ranges of the external applied voltage and electron energy. To our knowledge, this is the first demonstration of phase locking due to proximity effect induced torques in FMI/TI systems, justifying further investigation of these systems in terms of their possible role in serving as the fundamental building block of unconventional computing paradigms.

Some realistic considerations are the following. In an experimental setup, if the two FMIs are far from each other (e.g., $>$ 100 nm), scattering from impurities will destroy the coherence between the states of the two FMIs. In this case, our non-coherent approach is applicable. If the two FMIs are close to each other (e.g., within 100 nm), coherence cannot be ignored, rendering necessary our quantum coherence based treatment.

Direct interaction between the two FMIs can also affect the phase locking dynamics. One such type is the dipole-dipole interaction[31] described by the Hamiltonian

$$H_{dip} = -\frac{\mu_0}{4\pi|\boldsymbol{r}|^3}[3(\boldsymbol{m}_1 \cdot \hat{\boldsymbol{r}})(\boldsymbol{m}_2 \cdot \hat{\boldsymbol{r}}) - \boldsymbol{m}_1 \cdot \boldsymbol{m}_2], \quad (14)$$

where μ_0 is the vacuum permeability, $\boldsymbol{r}$ is the distance between the two effective point dipoles, $\hat{\boldsymbol{r}}$ is a unit vector parallel to the line joining the centers of the two dipoles, and $\boldsymbol{m}_{1,2} = \boldsymbol{M}_{1,2} \cdot V$ with V being the volume of the FMI stripe. For one FMI, the effective magnetic field from the second FMI is $\boldsymbol{B}_{1,2} = -\partial H/\partial \boldsymbol{M}_{1,2}$. Setting the two magnetization vectors in the same direction (the configuration of minimum energy) and using our simulation parameter setting, we estimate the energy density to be $H/V \approx 2\times10^4$ erg/cm^3 for $|\boldsymbol{r}| = 20$ nm. This is about one order of magnitude smaller than the anisotropy coefficient in the z direction ($K_z = 2.5\times10^5$ erg/cm^3). Insofar as the edge distance between the two FMIs is larger than 20 nm, dipole-dipole interaction can be neglected. If the two FMIs are too close to each other, the dipole-dipole energy can be comparable to the system energy, which cannot be ignored. The effect of dipole-dipole interaction on phase locking is a topic that warrants further study.

ACKNOWLEDGEMENT

We thank Prof. L. Huang for helpful discussions. We would like to acknowledge support from the Vannevar Bush Faculty Fellowship program sponsored by the Basic Research Office of the Assistant Secretary of Defense for Research and Engineering and funded by the Office of Naval Research through Grant No. N00014-16-1-2828.

Appendix A: Experimental realizability of phase locking in the FMI/TI heterostructure

A typical TI/FMI system is the Bi_2Se_3/YIG (yttrium iron garnet) heterostructure[69,75,76], where the effect of exchange interaction between the FMI and the TI surface states on the magnetization dynamics of YIG has been studied recently[76]. Among the different types of anisotropy in the YIG thin film, shape anisotropy is dominant. In particular, the hard axis is perpendicular to the plane of the film (z direction in our study) and the associated anisotropy coefficient is on the order of $K_z \sim 10^5$ erg/cm^3 when the thickness d of the film is in the range from several nm to tens of nm[75,76]. The magnetocrystalline anisotropy coefficient is smaller than that of the shape anisotropy, which is about $K \sim 2.5\times10^4$ erg/cm^3 and can produce a hard axis in the plane favoring magnetization along the $\langle 111\rangle$ axis[75]. The typical value of the magnetization is on the order of 1000 Oe[75,76]. Another widely studied heterostructure Bi_2Se_3/EuS[71,77–79], where progress on magnetoresistance and current-induced magnetization switching has been recently reported[79]. For EuS, the hard axis anisotropy is in the range[77,78] of $10^4 - 10^5$ erg/cm^3, and the value of magnetization[78] is also on the order of 1000 Oe. The anisotropy value used in our study, $K_z = 2.5\times10^5$ erg/cm^3, is comparable to those of the two materials. It is thus potentially feasible to realize auto-oscillation and then phase locking using the Bi_2Se_3/YIG or the Bi_2Se_3/EuS heterostructure.

While we have used specific anisotropy values to illustrate the phase locking phenomenon in the main text, these values can be tuned in certain ranges without losing phase locking, making it possible to match the values to those of real materials. Specifically, if the value of anisotropy in the z direction is fixed, phase locking can be achieved by varying the value of the anisotropy in the y direction and the applied voltage in a wide range. For example, say the anisotropy coefficient in the z direction is $K_z = 2.5\times10^5$ erg/cm^3. We find that phase locking can be achieved when the K_y value varies in a wide range and the voltage V can also be chosen from a range, as shown in Fig. 11, where the electron Fermi energy is $E = 100$ meV. The yellow area in Fig. 11 indicates the approximate parameter region for phase locking. We find, however, that it is necessary to restrict the anisotropy difference of the two nanocontacts to being less than 10% of the K_z value in order to realize phase locking.

The value of K_z can also be tunned without losing phase locking, which can be seen from the following heuristic analysis based on the LLG equation. Note that the LLG equation can be reduced to the Landau-Lifshitz (LL) equation by substituting the cross product of $\boldsymbol{n}$ on the left side

$$\boldsymbol{n} \times \frac{d\boldsymbol{n}}{dt} = -\gamma \boldsymbol{n} \times (\boldsymbol{n} \times \boldsymbol{B}_{eff}) - \alpha \frac{d\boldsymbol{n}}{dt}, \quad (A1)$$

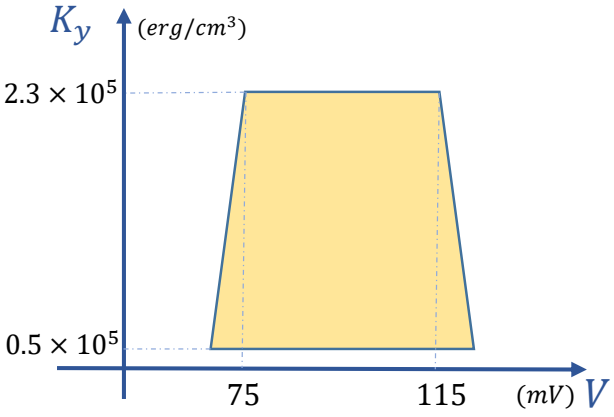


FIG. 11. **Typicality of phase locking in a representative parameter space**. For fixed $K_z = 2.5 \times 10^5$ erg/cm^3 and Fermi energy $E = 100$ meV, the region in the parameter plane (K_y, V) for phase locking (the yellow area).

into the LLG equation. We have

$$\frac{d\boldsymbol{n}}{dt} = -\frac{\gamma}{1+\alpha^2}\boldsymbol{n} \times \boldsymbol{B}_{eff} - \frac{\gamma\alpha}{1+\alpha^2}\boldsymbol{n} \times (\boldsymbol{n} \times \boldsymbol{B}_{eff}). \tag{A2}$$

In general, increasing the effective magnetic field is equivalent to decreasing the time period of magnetization oscillations. Specifically, we have $\boldsymbol{B}_{eff} = \boldsymbol{B}_{spin} + \boldsymbol{B}_{an}$, where the spin induced effective magnetic field is proportional to the applied voltage: $\boldsymbol{B}_{spin} \sim V$, and the anisotropic magnetic field is proportional to the anisotropy coefficient: $\boldsymbol{B}_{an} \sim K$. When the value of the material anisotropy is altered, say, within one order of magnitude, it is just necessary to change the voltage by the same amount to ensure that the value of $\boldsymbol{B}_{eff}$ changes by a proper amount. With such parameter changes, while the oscillation period or the characteristic time scale underlying the magnetization dynamics is changed, phase locking is maintained.

Appendix B: Iterative solution method for solving the coupled magnetization dynamics

Figure 12 presents a flow chart detailing our iterative procedure for solving the coupled LLG equations for the magnetization dynamics for the two cases where quantum interference is absent and present, respectively. All the quantities have been defined in Sec. II.

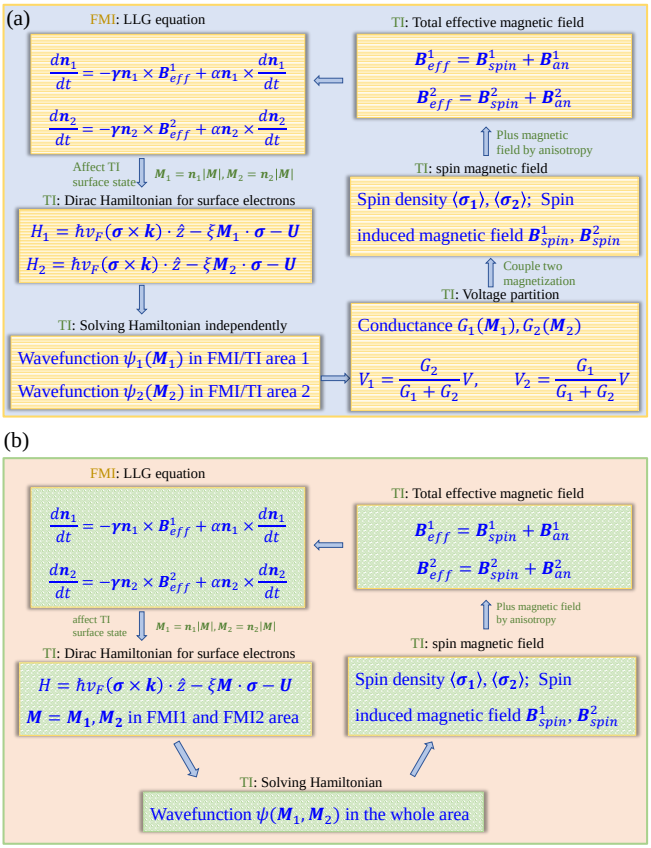


FIG. 12. **Iterative procedure for solving the coupled LLG equations for the magnetization dynamics**. The two FMIs are coupled by the surface current of the TI. (a,b) Without and with quantum interference, respectively.

Appendix C: Electron spin density calculation

1. Proof of an equality

We prove the equality

$$T_{\boldsymbol{M}}(E_F, \theta)\cos\theta = -\psi^\dagger \sigma_y \psi.$$

For one FMI/TI heterostructure (regions I, II and III in Fig. 9), the wavefunctions in the incident area, heterostructure interface, and the transmitted regions are[61], respectively,

$$\psi_1(x \le 0) = \frac{1}{\sqrt{2}}\begin{pmatrix} ie^{-i\theta} \\ 1 \end{pmatrix} e^{ik_F x\cos\theta} + \frac{r}{\sqrt{2}}\begin{pmatrix} -ie^{i\theta} \\ 1 \end{pmatrix} e^{-ik_F x\cos\theta}$$

$$\psi_2(0 < x < d) = A \cdot \begin{pmatrix} \hbar v_F(\tilde{k}_y + i\tilde{k}_x) \\ E + U - \xi M_z \end{pmatrix} e^{i(\tilde{k}_x + \xi M_y/\hbar v_F)x} + B \cdot \begin{pmatrix} \hbar v_F(\tilde{k}_y - i\tilde{k}_x) \\ E + U - \xi M_z \end{pmatrix} e^{i(-\tilde{k}_x + \xi M_y/\hbar v_F)x} \tag{C1}$$

$$\psi_3(x \geq d) = \frac{t}{\sqrt{2}} \begin{pmatrix} ie^{-i\theta} \\ 1 \end{pmatrix} e^{ik_F x \cos\theta} \tag{C2}$$

where r and t are the reflection and transmission coefficients, $E + U = \hbar v_F k_F$, $k_x = k_F \cos\theta$, $k_y = k_F \sin\theta$, $\hbar v_F \tilde{k}_x = \sqrt{(E+U)^2 - (\xi M_z)^2 - (\hbar v_F \tilde{k}_y)^2}$, and $\hbar v_F \tilde{k}_y = \hbar v_F k_y - \xi M_x$. For convenience, we denote $A = \frac{a}{\sqrt{2(E+U)(E+U-\xi M_z)}}$ and $B = \frac{b}{\sqrt{2(E+U)(E+U-\xi M_z)}}$ with a and b being the corresponding coefficients. Matching the wavefunctions at the boundary between different regions, we get the corresponding coefficients, r, a, b, and t. For simplicity, in the wavefunction expressions, the spatial normalization factor $1/\sqrt{LW}$ is not included, where L and W are the size parameters of the 2D device. For an electron, the y component of the spin in the transmitted region III can be obtained via the wavefunction [Eq. (C2)] average

$$\psi_3^\dagger \sigma_y \psi_3 = -|t|^2 \cos\theta, \tag{C3}$$

The transmission probability is $T(E,\theta) = |t|^2$. We have $T\cos\theta = -\psi_3^\dagger \sigma_y \psi_3$, which is the relation between electron transmission in the x direction and the y component of the spin in the transmitted region (free region), i.e., spin-momentum locking. In fact, this relation is also valid in the FMI/TI heterostructure region, i.e., $\psi_2^\dagger \sigma_y \psi_2 = \psi_3^\dagger \sigma_y \psi_3$ holds independent of position x, which can be proved, as follows. We write down the spin value in terms of the wavefunction [Eq. (C1)] in the heterostructure region at position x as

$$\begin{aligned} \psi_2^\dagger \sigma_y \psi_2 = &-2\beta \cdot \Big[|A|^2 \Im(\alpha_1) \exp(-2\Im(\tilde{k}_x)x) \\ &+ |B|^2 \Im(\alpha_2) \exp(2\Im(\tilde{k}_x)x) \Big] \\ &+ 2\beta \cdot \Re\Big[iA^* B \cdot (\alpha_2 - \alpha_1^*) \exp(-2i\Re(\tilde{k}_x)x) \Big] \end{aligned} \tag{C4}$$

where $\alpha_1 \equiv \hbar v_F(\tilde{k}_y + i\tilde{k}_x)$, $\alpha_2 \equiv \hbar v_F(\tilde{k}_y - i\tilde{k}_x)$, $\beta \equiv E + U - \xi M_z$, $\Re(\cdot)$ and $\Im(\cdot)$ represent the real and imaginary parts, respectively. The expression in Eq. (C4) can be further simplified. Note that $\tilde{k}_y$ is real and $\tilde{k}_x$ can be real or purely imaginary depending on the quantities M_z and k_y [c.f., $\hbar v_F \tilde{k}_x = \sqrt{(E+U)^2 - (\xi M_z)^2 - (\hbar v_F \tilde{k}_y)^2}$]. To evaluate the value of $\psi_2^\dagger \sigma_y \psi_2$, we first assume $\tilde{k}_x$ is real. In this case, the second part on the right-hand side of Eq. (C4) is zero, and $\exp(-2\Im(\tilde{k}_x)x) = \exp(2\Im(\tilde{k}_x)x) = 1$. We thus have

$$\psi_2^\dagger \sigma_y \psi_2 = -2\beta \hbar v_F \tilde{k}_x (|A|^2 - |B|^2), \tag{C5}$$

which is independent of the position x. We then consider the case where $\tilde{k}_x$ is purely imaginary. In this case, the first part on the right-hand side of Eq. (C4) is zero, because $\Im(\alpha_1) = \Im(\alpha_2) = 0$. Using $\exp(-2i\Re(\tilde{k}_x x)) = 1$, we have

$$\psi_2^\dagger \sigma_y \psi_2 = 4\beta \Re(A^* B \tilde{k}_x). \tag{C6}$$

which is also independent of position x. Utilizing wavefunction matching at the boundary, we see that the equality $T(E,\theta)\cos\theta = -\psi_3^\dagger \sigma_y \psi_3 = -\psi_2^\dagger \sigma_y \psi_2$ holds in the heterostructure region.

2. Calculation of the spin density

The current density along the x direction [Eq. (4)] can be written in terms of the spin average, i.e.,

$$J_x = \frac{V_1 G_1}{L_w} = -\frac{Ee^2 V_1}{2\pi^2 \hbar^2 v_F} \int_{-\frac{\pi}{2}}^{\frac{\pi}{2}} \psi_2^\dagger \sigma_y \psi_2 d\theta. \tag{C7}$$

Utilizing the current definition in the free area: $\hat{J} = -e\nabla_{\boldsymbol{p}} H = -ev_F(-\hat{\sigma}_y, \hat{\sigma}_x)$, we get the mean spin density as

$$\begin{aligned} \langle \sigma_y \rangle_1 &= \frac{J_x}{ev_F} = -\frac{EeV_1}{2\pi^2 \hbar^2 v_F^2} \int_{-\frac{\pi}{2}}^{\frac{\pi}{2}} \psi_3^\dagger \sigma_y \psi_3 d\theta \\ &= -\frac{EeV_1}{2\pi^2 \hbar^2 v_F^2} \int_{-\frac{\pi}{2}}^{\frac{\pi}{2}} \psi_2^\dagger \sigma_y \psi_2 d\theta \\ &= -\frac{EeV_1}{2\pi^2 \hbar^2 v_F^2 d} \int_0^d \int_{-\frac{\pi}{2}}^{\frac{\pi}{2}} \psi_2^\dagger \sigma_y \psi_2 d\theta dx. \end{aligned} \tag{C8}$$

For an incident electron with certain angle and energy, the spin value at each point x in the heterostructure is given by $(\psi_2^\dagger \sigma_x \psi_2, \psi_2^\dagger \sigma_y \psi_2, \psi_2^\dagger \sigma_z \psi_2)$. We perform the angle and position averages for σ_x and σ_z as for σ_y, and multiply the factor related to the electron density, as in Eq. (C8). The x and z components of the spin density in the heterostructure region can then be obtained by substituting $\psi_2^\dagger \sigma_y \psi_2$ with $\psi_2^\dagger \sigma_x \psi_2$ and $\psi_2^\dagger \sigma_z \psi_2$ in Eq. (C8):

$$\langle \sigma_x \rangle_1 = -\frac{EeV_1}{2\pi^2 \hbar^2 v_F^2 d} \int_0^d \int_{-\frac{\pi}{2}}^{\frac{\pi}{2}} \psi^\dagger \sigma_x \psi d\theta dx, \tag{C9}$$

$$\langle \sigma_z \rangle_1 = -\frac{EeV_1}{2\pi^2 \hbar^2 v_F^2 d} \int_0^d \int_{-\frac{\pi}{2}}^{\frac{\pi}{2}} \psi^\dagger \sigma_z \psi d\theta dx. \tag{C10}$$

3. Spin density in a 2D Rashba plane

The general Rashba Hamiltonian with exchange interaction has the form[80–82]

$$H = \frac{\hbar^2}{2m} k^2 + \alpha(\boldsymbol{\sigma} \times \boldsymbol{k}) \cdot \hat{z} - \xi \boldsymbol{M} \cdot \boldsymbol{\sigma}, \tag{C11}$$

where $\hbar \boldsymbol{k} = -i\hbar(\partial_x, \partial_y, 0)$ is the two-dimensional electron momentum operator, α parametrizes the spin-orbit coupling, ξ is the exchange coupling strength between conduction electron and magnetization. We can write down the wavefunctions in the incident, heterostructure and transmitted areas, and match the wavefunctions at the boundary to get the corresponding coefficients. For

example, for the transmitted wave in the following form[83] (which is needed for calculating the spin density):

$$\phi_t = \frac{t}{\sqrt{2}} \exp(i\boldsymbol{k}\cdot\boldsymbol{r}) \cdot \begin{pmatrix} i\cdot s\exp(-i\theta) \\ 1 \end{pmatrix} \tag{C12}$$

where t is the transmission coefficient, $s = \pm 1$, and $\exp(-i\theta) = (k_x - ik_y)/\sqrt{k_x^2 + k_y^2}$. The current operator in the x direction in the transmitted area is defined as

$$\hat{J}_x = -e\nabla_{p_x} H = -e(\frac{p_x}{m} - \frac{\alpha}{\hbar}\hat{\sigma}_y). \tag{C13}$$

For an electron, the current with incident angle θ is

$$\begin{aligned} j_x = \phi_t^\dagger \hat{J}_x \phi_t &= -e\Big[\frac{p_x}{m}|t|^2 + s\cdot\frac{\alpha}{\hbar}|t|^2\cos\theta\Big] \\ &= -e\Big[\frac{\hbar k}{m} + \frac{s\alpha}{\hbar}\Big]|t|^2\cos\theta \end{aligned} \tag{C14}$$

The angle averaged current is

$$j_x^{ave} = \frac{-e}{\pi}\cdot\Big[\frac{\hbar k}{m} + \frac{s\alpha}{\hbar}\Big]\int_{-\frac{\pi}{2}}^{\frac{\pi}{2}} T_{\boldsymbol{M}}(E,\theta)\cos\theta d\theta. \tag{C15}$$

From the classical Landauer-Buttiker formalism[58,62,74], we have the conductance as

$$G = \frac{Ee^2 L_w}{2\pi^2\hbar^2 v_F}\int_{-\frac{\pi}{2}}^{\frac{\pi}{2}} T_{\boldsymbol{M}}(E,\theta)\cos\theta d\theta. \tag{C16}$$

The current density is

$$J_x = \frac{V_1 G_1}{L_w} = \frac{Ee^2 V_1}{2\pi\hbar^2 v_F}\cdot\frac{1}{\pi}\int_{-\frac{\pi}{2}}^{\frac{\pi}{2}} T_{\boldsymbol{M}}(E,\theta)\cos\theta d\theta. \tag{C17}$$

The incident electron density can then be expressed as

$$n = \frac{J_x}{j_x^{ave}} = -\frac{EeV_1}{2\pi\hbar^2 v_F}\cdot\frac{1}{\frac{\hbar k}{m} + \frac{s\alpha}{\hbar}}. \tag{C18}$$

Once the current density is obtained, we can calculate the spin average over different incident angles and positions. For example, the σ_y component can be written as

$$\begin{aligned} \langle\sigma_y\rangle_1 &= n\cdot\frac{1}{\pi d}\int_0^d\int_{-\frac{\pi}{2}}^{\frac{\pi}{2}} \psi^\dagger\sigma_y\psi d\theta dx \\ &= -\frac{EeV_1}{2\pi^2\hbar^2 v_F d}\cdot\frac{1}{\frac{\hbar k}{m} + \frac{s\alpha}{\hbar}}\int_0^d\int_{-\frac{\pi}{2}}^{\frac{\pi}{2}} \psi^\dagger\sigma_y\psi d\theta dx, \end{aligned} \tag{C19}$$

Taking the limit $m\to\infty$, $\alpha = \hbar v_F$, $s = 1$, we get the spin density for our TI system in Eq. (C8). That is, the surface states of TI correspond to the $m\to\infty$ limit of the 2D Rashba Hamiltonian, at which the maximum spin-momentum locking efficiency is achieved.

Another type of 2D Rashba systems can be graphene based heterostructures, e.g., graphene/Ni(111) and graphene/transition metal dichalcogenide. For such systems, the electron dynamics are governed by the 2D Dirac-Rashba Hamiltonian and exhibit significant in-plane spin polarization, which is perpendicular to electron momentum and proportional to the group velocity[84]. Similar to the surface electron states of a topological insulator, an in-plane voltage induced charge current will produce a spin density along the perpendicular direction and hence a torque that can be the driven source for magnetization in adjacent magnetic insulators. Generalizing the current formalism, we expect similar inter-coupling dynamics between electronic transport and magnetization.

Appendix D: Solutions of quantum tunneling of Dirac electrons through double FMI barriers

The spinor wavefunctions in the five regions in Fig. 9 can be written as

$$\begin{aligned} \psi_1(x\le 0) = &\frac{1}{\sqrt{2}}\begin{pmatrix} ie^{-i\theta} \\ 1 \end{pmatrix} e^{ik_F x\cos\theta} \\ &+\frac{r}{\sqrt{2}}\begin{pmatrix} -ie^{i\theta} \\ 1 \end{pmatrix} e^{-ik_F x\cos\theta} \end{aligned}$$

$$\begin{aligned} \psi_2(0<x\le d) = &\frac{1}{\sqrt{2(E+U_1)(E+U_1-M_{z1})}} \\ &\cdot\Bigg[a\begin{pmatrix} \hbar v_F(\tilde{k}_{y1} + i\tilde{k}_{x1}) \\ E+U_1-M_{z1} \end{pmatrix} e^{i(\tilde{k}_{x1}+m_{y1}/\hbar v_F)x} \\ &+b\begin{pmatrix} \hbar v_F(\tilde{k}_{y1} - i\tilde{k}_{x1}) \\ E+U_1-M_{z1} \end{pmatrix} e^{i(-\tilde{k}_{x1}+m_{y1}/\hbar v_F)x}\Bigg] \end{aligned}$$

$$\begin{aligned} \psi_3(d<x<L+d) = &\frac{c}{\sqrt{2}}\begin{pmatrix} ie^{-i\theta} \\ 1 \end{pmatrix} e^{ik_F x\cos\theta} \\ &+\frac{d}{\sqrt{2}}\begin{pmatrix} -ie^{i\theta} \\ 1 \end{pmatrix} e^{-ik_F x\cos\theta} \end{aligned}$$

$$\begin{aligned} \psi_4(L+d<x<L+2d) = &\frac{1}{\sqrt{2(E+U_2)(E+U_2-M_{z2})}} \\ &\cdot\Bigg[f\begin{pmatrix} \hbar v_F(\tilde{k}_{y2} + i\tilde{k}_{x2}) \\ E+U_2-M_{z2} \end{pmatrix} e^{i(\tilde{k}_{x2}+m_{y2}/\hbar v_F)x} \\ &+g\begin{pmatrix} \hbar v_F(\tilde{k}_{y2} - i\tilde{k}_{x2}) \\ E+U_2-M_{z2} \end{pmatrix} e^{i(-\tilde{k}_{x2}+m_{y2}/\hbar v_F)x}\Bigg] \end{aligned}$$

$$\psi_5(L+2d<x) = \frac{t}{\sqrt{2}}\begin{pmatrix} ie^{-i\theta} \\ 1 \end{pmatrix} e^{ik_F x\cos\theta}$$

where r is the reflection coefficient in region I, t is the transmission coefficient in region V, a, b, c, d, f, and g

are the corresponding coefficients in regions II, III, and IV. Other quantities are

$$\begin{aligned}
E &= \hbar v_F k_F, \\
k_y &= k_F \sin\theta, \\
\hbar v_F \tilde{k}_{x1} &= \sqrt{E^2 - m_{z1}^2 - (\hbar v_F \tilde{k}_y)^2}, \\
\hbar v_F \tilde{k}_{x2} &= \sqrt{E^2 - m_{z2}^2 - (\hbar v_F \tilde{k}_y)^2}, \\
\hbar v_F \tilde{k}_{y1} &= \hbar v_F k_y + m_{x1}, \\
\hbar v_F \tilde{k}_{y2} &= \hbar v_F k_y + m_{x2},
\end{aligned}$$

U_1 and U_2 are the biases applied on the two FMIs, respectively, and $\boldsymbol{m} = \xi \boldsymbol{M}$. Matching the wavefunctions at the boundaries, we get all the coefficients and hence the wavefunction in the whole domain, as follows.

$$t = \frac{Z_5 Z_{10} - Z_6 Z_9}{(Z_4 Z_{10} - Z_6 Z_8) b_0 - (Z_6 Z_7 - Z_3 Z_1 0) a_0},$$

$$r = \frac{(Z_5 Z_7 - Z_3 Z_9) a_0 - (Z_4 Z_9 - Z_5 Z_8) b_0}{(Z_4 Z_{10} - Z_6 Z_8) b_0 - (Z_6 Z_7 - Z_3 Z_{10}) a_0},$$

$$a = \frac{(Y_6 Z_1 - Y_7 Y_{10}) C_0 + (Y_6 Z_2 - Y_8 Y_{10}) d_0}{Y_6 Y_9 - Y_5 Y_{10}} t = a_0 t,$$

$$b = \frac{(Y_6 Y_9 - Y_5 Z_1) C_0 + (Y_8 Y_9 - Y_5 Z_2) d_0}{Y_6 Y_9 - Y_5 Y_{10}} t = b_0 t,$$

$$c = \frac{(X_{10} Y_1 - X_7 Y_4) f_0 + (X_{10} Y_2 - X_8 Y_4) g_0}{X_{10} Y_3 - X_9 Y_4} t = c_0 t,$$

$$d = \frac{(X_7 Y_3 - X_9 Y_1) f_0 + (X_8 Y_3 - X_9 Y_2) g_0}{X_{10} Y_3 - X_9 Y_4} t = d_0 t,$$

$$f = \frac{X_2 X_6 - X_3 X_5}{X_2 X_4 - X_1 X_5} t = f_0 t,$$

$$g = \frac{X_3 X_4 - X_1 X_6}{X_2 X_4 - X_1 X_5} t = g_0 t,$$

where th variables X_1-X_{10}, Y_1-Y_{10}, and Z_1-Z_{10} are

$$X_1 \equiv \hbar v_F (\tilde{k}_{y2} + i\tilde{k}_{x2}) e^{i(\tilde{k}_{x2} + m_{y2}/\hbar v_F)(L+2d)},$$

$$X_2 \equiv \hbar v_F (\tilde{k}_{y2} - i\tilde{k}_{x2}) e^{i(-\tilde{k}_{x2} + m_{y2}/\hbar v_F)(L+2d)},$$

$$X_3 \equiv i e^{-i\theta} e^{ik_F (L+2d)\cos\theta} \sqrt{(E+U_2)(E+U_2 - m_{z2})},$$

$$\begin{aligned}
X_4 &\equiv (E + U2 - m_{z2}) e^{i(\tilde{k}_{x2} + m_{y2}/\hbar v_F)(L+2d)}, \\
X_5 &\equiv (E + U2 - m_{z2}) e^{-i(\tilde{k}_{x2} + m_{y2}/\hbar v_F)(L+2d)},
\end{aligned}$$

$$X_6 \equiv e^{ik_F (L+2d)\cos\theta} \sqrt{(E+U_2)(E+U_2 - m_{z2})},$$

$$X_7 = e^{-ik_F (L+d)\cos\theta} \sqrt{(E+U_2)(E+U_2 - m_{z2})},$$

$$X_8 \equiv \hbar v_F (\tilde{k}_{y2} - i\tilde{k}_{x2}) e^{i(-\tilde{k}_{x2} + m_{y2}/\hbar v_F)(L+d)},$$

$$X_9 \equiv i e^{-i\theta} e^{ik_F (L+2d)\cos\theta} \sqrt{(E+U_2)(E+U_2 - m_{z2})},$$

$$X_{10} \equiv -i e^{-i\theta} e^{ik_F (L+2d)\cos\theta} \sqrt{(E+U_2)(E+U_2 - m_{z2})},$$

$$X_{10} \equiv -i e^{-i\theta} e^{ik_F (L+2d)\cos\theta} \sqrt{(E+U_2)(E+U_2 - m_{z2})},$$

$$Y_1 \equiv (E + U2 - m_{z2}) e^{i(\tilde{k}_{x2} + m_{y2}/\hbar v_F)(L+d)},$$

$$Y_2 \equiv (E + U2 - m_{z2}) e^{i(-\tilde{k}_{x2} + m_{y2}/\hbar v_F)(L+d)},$$

$$Y_3 \equiv e^{ik_F (L+d)\cos\theta} \sqrt{(E+U_2)(E+U_2 - m_{z2})},$$

$$Y_4 \equiv e^{-ik_F (L+d)\cos\theta} \sqrt{(E+U_2)(E+U_2 - m_{z2})},$$

$$Y_5 \equiv \hbar v_F (\tilde{k}_{y1} + i\tilde{k}_{x1}) e^{i(\tilde{k}_{x1} + m_{y1}/\hbar v_F) d},$$

$$Y_6 \equiv \hbar v_F (\tilde{k}_{y1} - i\tilde{k}_{x1}) e^{i(-\tilde{k}_{x1} + m_{y1}/\hbar v_F) d},$$

$$Y_7 \equiv i e^{-i\theta} e^{ik_F d\cos\theta} \sqrt{(E+U_1)(E+U_1 - m_{z1})},$$

$$Y_8 \equiv -i e^{-i\theta} e^{ik_F d\cos\theta} \sqrt{(E+U_1)(E+U_1 - m_{z1})},$$

$$Y_9 \equiv (E + U1 - m_{z1}) e^{i(\tilde{k}_{x1} + m_{y1}/\hbar v_F) d},$$

$$Y_1 0 \equiv (E + U1 - m_{z1}) e^{i(-\tilde{k}_{x1} + m_{y1}/\hbar v_F) d},$$

$$Z_1 \equiv e^{ik_F d\cos\theta} \sqrt{(E+U_1)(E+U_1 - m_{z1})},$$

$$Z_2 \equiv e^{-ik_F d\cos\theta} \sqrt{(E+U_1)(E+U_1 - m_{z1})},$$

$$Z_3 \equiv \hbar v_F (\tilde{k}_{y1} + i\tilde{k}_{x1}),$$

$$Z_4 \equiv \hbar v_F (\tilde{k}_{y1} - i\tilde{k}_{x1}),$$

$$Z_5 \equiv -Z_6 = i e^{-i\theta} \sqrt{(E+U_1)(E+U_1 - m_{z1})},$$

$$Z_7 \equiv Z_8 = E + U1 - m_{z1},$$

$$Z_9 \equiv Z_{10} = \sqrt{(E+U_1)(E+U_1 - m_{z1})},$$

* Ying-Cheng.Lai@asu.edu

[1] E. Goto, "New parametron circuit element using nonlinear reactance," KDD Kenyku Shiryo (1954).

[2] J. von Neumann, "Non-linear capacitance or inductance switching, amplifying, and memory organs," US Patent **US2815488** (1957).

[3] R. A. Kiehl and T. Ohshima, "Bistable locking of single-electron tunneling elements for digital circuitry," Appl. Phys. Lett. **67**, 2494 (1995).

[4] T. Ohshima and R. A. Kiehl, "Operation of bistable phase-locked single-electron tunneling logic elements," J. Appl. Phys. **80**, 912 (1996).

[5] E. M. Izhikevich, "Weakly pulse-coupled oscillators, fm interactions, synchronization, and oscillatory associative memory," IEEE Trans. Neu. Net. **10**, 508 (1999).

[6] J. S. Wu, L. C. Jiao, R. Li, and W. S. Chen, "Clustering dynamics of nonlinear oscillator network: Application to graph coloring problem," Physica D **240**, 1972 (2011).

[7] F. T. Leighton, "A graph coloring algorithm for large scheduling problems," J. Res. Natl. Bur. Stand. **84**, 489 (1979).

[8] T. K. Woo, S. Y. W. Su, and R. Newmanwolfe, "Resource-allocation in a dynamically partitionable bus network using a graph-coloring algorithm," IEEE Trans. Comm. **39**, 1794 (1991).

[9] A. Parihar, N. Shukla, M. Jerry, S. Datta, and A. Raychowdhury, "Vertex coloring of graphs via phase dynamics of coupled oscillatory networks," Sci. Rep. **7**, 911 (2017).

[10] F. Y. Liu, F. T. An, and R. A. Kiehl, "Ternary single electron tunneling phase logic element," Appl. Phys. Lett. **74**, 4040 (1999).

[11] T. Yang, R. A. Kiehl, and L. O. Chua, "Tunneling phase logic cellular nonlinear networks," Int. J. Bif. Chaos **11**, 2895 (2001).

[12] T. Li and R. Kiehl, "Operating regimes for multivalued single-electron tunneling phase logic," J. Appl. Phys. **93**, 9291 (2003).

[13] N. A. Nezlobin and R. A. Kiehl, "Phase-locking in a nonuniform array of tunnel junctions," J. Appl. Phys. **94**, 6841 (2003).

[14] R. A. Kiehl, "Information processing by nonlinear phase dynamics in locally connected arrays," arXiv preprint arXiv:1603.06665 (2016).

[15] J. C. Slonczewski, "Current-driven excitation of magnetic multilayers," J. Magn. Magn. Mater. **159**, L1 (1996).

[16] L. Berger, "Emission of spin waves by a magnetic multilayer traversed by a current," Phys. Rev. B **54**, 9353 (1996).

[17] D. C. Ralph and M. D. Stiles, "Spin transfer torques," J. Magn. Magn. Mater. **320**, 1190 (2008).

[18] A. Brataas, A. D. Kent, and H. Ohno, "Current-induced torques in magnetic materials," Nat. Mater. **11**, 372 (2012).

[19] S. I. Kiselev, J. Sankey, I. Krivorotov, N. Emley, R. Schoelkopf, R. Buhrman, and D. Ralph, "Microwave oscillations of a nanomagnet driven by a spin-polarized current," Nature **425**, 380 (2003).

[20] W. H. Rippard, M. R. Pufall, S. Kaka, S. E. Russek, and T. J. Silva, "Direct-current induced dynamics in c o 90 f e 10/n i 80 f e 20 point contacts," Phys. Rev. Lett. **92**, 027201 (2004).

[21] I. Krivorotov, N. Emley, J. Sankey, S. Kiselev, D. Ralph, and R. Buhrman, "Time-domain measurements of nanomagnet dynamics driven by spin-transfer torques," Science **307**, 228 (2005).

[22] S. Kaka, M. R. Pufall, W. H. Rippard, T. J. Silva, S. E. Russek, and J. A. Katine, "Mutual phase-locking of microwave spin torque nano-oscillators," Nature **437**, 389 (2005).

[23] F. Mancoff, N. Rizzo, B. Engel, and S. Tehrani, "Phase-locking in double-point-contact spin-transfer devices," Nature **437**, 393 (2005).

[24] A. Slavin and V. Tiberkevich, "Theory of mutual phase locking of spin-torque nanosized oscillators," Phys. Rev. B **74**, 104401 (2006).

[25] J. Grollier, V. Cros, and A. Fert, "Synchronization of spin-transfer oscillators driven by stimulated microwave currents," Phys. Rev. B **73**, 060409 (2006).

[26] J. Persson, Y. Zhou, and J. Akerman, "Phase-locked spin torque oscillators: Impact of device variability and time delay," J. Appl. Phys. **101**, 09A503 (2007).

[27] B. Georges, J. Grollier, V. Cros, and A. Fert, "Impact of the electrical connection of spin transfer nano-oscillators on their synchronization: an analytical study," Appl. Phys. Lett. **92**, 232504 (2008).

[28] D. Li, Y. Zhou, C. Zhou, and B. Hu, "Global attractors and the difficulty of synchronizing serial spin-torque oscillators," Phys. Rev. B **82**, 140407 (2010).

[29] S. Sani, J. Persson, S. M. Mohseni, Y. Pogoryelov, P. Muduli, A. Eklund, G. Malm, M. Käll, A. Dmitriev, and J. Åkerman, "Mutually synchronized bottom-up multi-nanocontact spin–torque oscillators," Nat. Comm. **4**, 2731 (2013).

[30] J. Turtle, P.-L. Buono, A. Palacios, C. Dabrowski, V. In, and P. Longhini, "Synchronization of spin torque nano-oscillators," Phys. Rev. B **95**, 144412 (2017).

[31] H.-H. Chen, C.-M. Lee, Z. Zhang, Y. Liu, J.-C. Wu, L. Horng, and C.-R. Chang, "Phase locking of spin-torque nano-oscillator pairs with magnetic dipolar coupling," Phys. Rev. B **93**, 224410 (2016).

[32] A. Ruotolo, V. Cros, B. Georges, A. Dussaux, J. Grollier, C. Deranlot, R. Guillemet, K. Bouzehouane, S. Fusil, and A. Fert, "Phase-locking of magnetic vortices mediated by antivortices," Nat. Nanotech. **4**, 528 (2009).

[33] T. Chen, R. K. Dumas, A. Eklund, P. K. Muduli, A. H. A. A. Awad, P. Dürrenfeld, B. G. Malm, A. Rusu, and J. Akerman, "Spin-torque and spin-hall nano-oscillators," Proc. IEEE **104**, 1919 (2016).

[34] M. Sharad, C. Augustine, and K. Roy, "Boolean and non-boolean computation with spin devices," in *IEEE International Electron Device Meeting (IEDM)*, Vol. 52 (IEEE, San Francisco, 2012) pp. 443–545.

[35] A. Horvath, F. Corinto, G. Csaba, W. Porod, and T. Roska, "Synchronization in cellular spin torque oscillator arrays," in *13th International Workshop on Cellular Nanoscale Networks and Their Applications (CNNA)* (IEEE, Turin Italy, 2012).

[36] G. Csaba and W. Porod, "Computational study of spin-torque oscillator interactions for non-boolean computing applications," IEEE Trans. Magnetics **49**, 4447 (2013).

[37] D. E. Nikonov, G. Csaba, W. Porod, T. Shibata, D. Voils, D. Hammerstrom, I. A. Young, and G. I. Bourianoff,

"Coupled-oscillator associative memory array operation for pattern recognition," IEEE J. Explor. Solid-State Comp. Dev. Cir. **1**, 85 (2015).
[38] D. Fan, S. Maji, K. Yogendra, M. Sharad, and K. Roy, "Injection-locked spin hall-induced coupled-oscillators for energy efficient associative computing," IEEE Trans. Nanotech. **14**, 1083 (2015).
[39] F. Maciá, F. C. Hoppensteadt, and A. Kent, "Spin wave excitation patterns generated by spin torque oscillators," Nanotech. **25**, 1045303 (2014).
[40] V. E. Demidov, S. Urazhdin, H. Ulrichs, V. Tiberkevich, A. Slavin, D. Baither, G. Schmitz, and S. O. Demokritov, "Magnetic nano-oscillator driven by pure spin current," Nat. Mater. **11**, 1028 (2012).
[41] L. Liu, C.-F. Pai, D. Ralph, and R. Buhrman, "Magnetic oscillations driven by the spin hall effect in 3-terminal magnetic tunnel junction devices," Phys. Rev. Lett. **109**, 186602 (2012).
[42] R. Liu, W. Lim, and S. Urazhdin, "Spectral characteristics of the microwave emission by the spin hall nano-oscillator," Phys. Rev. Lett. **110**, 147601 (2013).
[43] A. Giordano, M. Carpentieri, A. Laudani, G. Gubbiotti, B. Azzerboni, and G. Finocchio, "Spin-hall nano-oscillator: A micromagnetic study," Appl. Phys. Lett. **105**, 042412 (2014).
[44] V. Demidov, H. Ulrichs, S. Gurevich, S. Demokritov, V. Tiberkevich, A. Slavin, A. Zholud, and S. Urazhdin, "Synchronization of spin hall nano-oscillators to external microwave signals," Nat. Commun. **5**, 3179 (2014).
[45] M. Elyasi, C. S. Bhatia, and H. Yang, "Synchronization of spin-transfer torque oscillators by spin pumping, inverse spin hall, and spin hall effects," J. Appl. Phys. **117**, 063907 (2015).
[46] T. Qu and R. Victora, "Phase-lock requirements in a serial array of spin transfer nano-oscillators," Sci. Rep. **5**, 11462 (2015).
[47] M. Z. Hasan and C. L. Kane, "Colloquium: topological insulators," Rev. Mod. Phys. **82**, 3045 (2010).
[48] X.-L. Qi and S.-C. Zhang, "Topological insulators and superconductors," Rev. Mod. Phys. **83**, 1057 (2011).
[49] Y. Shiomi, K. Nomura, Y. Kajiwara, K. Eto, M. Novak, K. Segawa, Y. Ando, and E. Saitoh, "Spin-electricity conversion induced by spin injection into topological insulators," Phys. Rev. Lett. **113**, 196601 (2014).
[50] P. Deorani, J. Son, K. Banerjee, N. Koirala, M. Brahlek, S. Oh, and H. Yang, "Observation of inverse spin hall effect in bismuth selenide," Phys. Rev. B **90**, 094403 (2014).
[51] M. Jamali, J. S. Lee, J. S. Jeong, F. Mahfouzi, Y. Lv, Z. Zhao, B. K. Nikolic, K. A. Mkhoyan, N. Samarth, and J.-P. Wang, "Giant spin pumping and inverse spin hall effect in the presence of surface and bulk spin- orbit coupling of topological insulator bi2se3," Nano Lett. **15**, 7126 (2015).
[52] J.-C. Rojas-Sánchez, S. Oyarzún, Y. Fu, A. Marty, C. Vergnaud, S. Gambarelli, L. Vila, M. Jamet, Y. Ohtsubo, A. Taleb-Ibrahimi, P. Le Fèvre, F. Bertran, N. Reyren, J.-M. George, and A. Fert, "Spin to charge conversion at room temperature by spin pumping into a new type of topological insulator: α-sn films," Phys. Rev. Lett. **116**, 096602 (2016).
[53] Y. Fan, X. Kou, P. Upadhyaya, Q. Shao, L. Pan, M. Lang, X. Che, J. Tang, M. Montazeri, K. Murata, L.-T. Chang, M. Akyol, G.-Q. Yu, T.-X. Nie, K. L. Wong, J. Liu, Y. Wang, Y. Tserkovnyak, and K. L. Wang, "Electric-field control of spin–orbit torque in a magnetically doped topological insulator," Nat. Nanotechnol. **11**, 352 (2016).
[54] Y. Wang, P. Deorani, K. Banerjee, N. Koirala, M. Brahlek, S. Oh, and H. Yang, "Topological surface states originated spin-orbit torques in bi 2 se 3," Phys. Rev. Lett. **114**, 257202 (2015).
[55] A. Mellnik, J. Lee, A. Richardella, J. Grab, P. Mintun, M. H. Fischer, A. Vaezi, A. Manchon, E.-A. Kim, N. Samarth, *et al.*, "Spin-transfer torque generated by a topological insulator," Nature **511**, 449 (2014).
[56] Y. Fan, P. Upadhyaya, X. Kou, M. Lang, S. Takei, Z. Wang, J. Tang, L. He, L.-T. Chang, M. Montazeri, *et al.*, "Magnetization switching through giant spin–orbit torque in a magnetically doped topological insulator heterostructure," Nat. Mater. **13**, 699 (2014).
[57] T. Yokoyama, Y. Tanaka, and N. Nagaosa, "Anomalous magnetoresistance of a two-dimensional ferromagnet/ferromagnet junction on the surface of a topological insulator," Phys. Rev. B **81**, 121401 (2010).
[58] Z. Wu, F. Peeters, and K. Chang, "Electron tunneling through double magnetic barriers on the surface of a topological insulator," Phys. Rev. B **82**, 115211 (2010).
[59] I. Garate and M. Franz, "Inverse spin-galvanic effect in the interface between a topological insulator and a ferromagnet," Phys. Rev. Lett. **104**, 146802 (2010).
[60] T. Yokoyama, J. Zang, and N. Nagaosa, "Theoretical study of the dynamics of magnetization on the topological surface," Phys. Rev. B **81**, 241410 (2010).
[61] T. Yokoyama, "Current-induced magnetization reversal on the surface of a topological insulator," Phys. Rev. B **84**, 113407 (2011).
[62] Y. G. Semenov, X. Duan, and K. W. Kim, "Voltage-driven magnetic bifurcations in nanomagnet–topological insulator heterostructures," Phys. Rev. B **89**, 201405 (2014).
[63] X. Duan, X.-L. Li, Y. G. Semenov, and K. W. Kim, "Nonlinear magnetic dynamics in a nanomagnet–topological insulator heterostructure," Phys. Rev. B **92**, 115429 (2015).
[64] P. B. Ndiaye, C. A. Akosa, M. H. Fischer, A. Vaezi, E.-A. Kim, and A. Manchon, "Dirac spin-orbit torques and charge pumping at the surface of topological insulators," Phys. Rev. B **96**, 014408 (2017).
[65] G. Wang, H. Xu, and Y.-C. Lai, "Nonlinear dynamics induced anomalous hall effect in topological insulators," Sci. Rep. **6**, 19803 (2016).
[66] G. Wang, H. Xu, and Y.-C. Lai, "Emergence, evolution, and control of multistability in a hybrid topological quantum/classical system," Chaos **28**, 033601 (2018).
[67] A. Richardella, A. Kandala, and N. Samarth, "Topological insulator thin films and heterostructures: Epitaxial growth, transport, and magnetism," in *Topological Insulators: Fundamentals and Perspectives* (John Wiley & Sons, 2015) pp. 295–329.
[68] F. Hellman, A. Hoffmann, Y. Tserkovnyak, G. S. Beach, E. E. Fullerton, C. Leighton, A. H. MacDonald, D. C. Ralph, D. A. Arena, H. A. Dürr, *et al.*, "Interface-induced phenomena in magnetism," Rev. Mod. Phys. **89**, 025006 (2017).
[69] M. Lang, M. Montazeri, M. C. Onbasli, X. Kou, Y. Fan, P. Upadhyaya, K. Yao, F. Liu, Y. Jiang, W. Jiang, *et al.*, "Proximity induced high-temperature magnetic order in topological insulator-ferrimagnetic insulator heterostructure," Nano Lett. **14**, 3459 (2014).
[70] A. Kandala, A. Richardella, D. Rench, D. Zhang, T. Flanagan, and N. Samarth, "Growth and characterization of

hybrid insulating ferromagnet-topological insulator heterostructure devices," Appl. Phys. Lett. **103**, 202409 (2013).

[71] P. Wei, F. Katmis, B. A. Assaf, H. Steinberg, P. Jarillo-Herrero, D. Heiman, and J. S. Moodera, "Exchange-coupling-induced symmetry breaking in topological insulators," Phys. Rev. Lett. **110**, 186807 (2013).

[72] Q. I. Yang, M. Dolev, L. Zhang, J. Zhao, A. D. Fried, E. Schemm, M. Liu, A. Palevski, A. F. Marshall, S. H. Risbud, *et al.*, "Emerging weak localization effects on a topological insulator–insulating ferromagnet (bi 2 se 3-eus) interface," Phys. Rev. B **88**, 081407 (2013).

[73] L. Alegria, H. Ji, N. Yao, J. Clarke, R. Cava, and J. Petta, "Large anomalous hall effect in ferromagnetic insulator-topological insulator heterostructures," Appl. Phys. Lett. **105**, 053512 (2014).

[74] S. Datta, *Electronic Transport in Mesoscopic Systems* (Cambridge University Press, Cambridge, England, 1995).

[75] H. Wang, J. Kally, J. S. Lee, T. Liu, H. Chang, D. R. Hickey, K. A. Mkhoyan, M. Wu, A. Richardella, and N. Samarth, "Surface-state-dominated spin-charge current conversion in topological-insulator–ferromagnetic-insulator heterostructures," Phys. Rev. Lett. **117**, 076601 (2016).

[76] Y. Fanchiang, K. Chen, C. Tseng, C. Chen, C. Cheng, S. Yang, C. Wu, S. Lee, M. Hong, and J. Kwo, "Strongly exchange-coupled and surface-state-modulated magnetization dynamics in bi 2 se 3/yttrium iron garnet heterostructures," Nat. Comm. **9**, 223 (2018).

[77] M. Li, C.-Z. Chang, B. J. Kirby, M. E. Jamer, W. Cui, L. Wu, P. Wei, Y. Zhu, D. Heiman, J. Li, *et al.*, "Proximity-driven enhanced magnetic order at ferromagnetic-insulator–magnetic-topological-insulator interface," Phys. Rev. Lett. **115**, 087201 (2015).

[78] F. Katmis, V. Lauter, F. S. Nogueira, B. A. Assaf, M. E. Jamer, P. Wei, B. Satpati, J. W. Freeland, I. Eremin, D. Heiman, *et al.*, "A high-temperature ferromagnetic topological insulating phase by proximity coupling," Nature **533**, 513 (2016).

[79] Y. Lv, J. Kally, T. Liu, P. Sahu, M. Wu, N. Samarth, and J.-P. Wang, "Large unidirectional spin hall and rashba-edelstein magnetoresistance in topological insulator/magnetic insulator heterostructures," arXiv preprint arXiv:1806.09066 (2018).

[80] A. Manchon and S. Zhang, "Theory of nonequilibrium intrinsic spin torque in a single nanomagnet," Phys. Rev. B **78**, 212405 (2008).

[81] A. Manchon and S. Zhang, "Theory of spin torque due to spin-orbit coupling," Phys. Rev. B **79**, 094422 (2009).

[82] I. M. Miron, G. Gaudin, S. Auffret, B. Rodmacq, A. Schuhl, S. Pizzini, J. Vogel, and P. Gambardella, "Current-driven spin torque induced by the rashba effect in a ferromagnetic metal layer," Nat. Mater. **9**, 230 (2010).

[83] J.-I. Inoue, G. E. Bauer, and L. W. Molenkamp, "Diffuse transport and spin accumulation in a rashba two-dimensional electron gas," Phys. Rev. B **67**, 033104 (2003).

[84] E. I. Rashba, "Graphene with structure-induced spin-orbit coupling: Spin-polarized states, spin zero modes, and quantum hall effect," Phys. Rev. B **79**, 161409 (2009).